J. Fluid Mech. (1994), *vol.* 275, *pp.* 59–81

Critical points in a turbulent near wake

By Y. ZHOU AND R. A. ANTONIA
Department of Mechanical Engineering, University of Newcastle, NSW 2308, Australia

(Received 2 February 1993 and in revised form 14 March 1994)

Velocity data were obtained in the turbulent wake of a circular cylinder with an orthogonal array of sixteen X-wires, eight in the (x, y)-plane and eight in the (x, z)-plane. By applying the phase-plane technique to these data, three types of critical points (where the velocity is zero and the streamline slope is indeterminate) were identified. Of these, foci and saddle points occurred most frequently, although a significant number of nodes was also found. Flow topology and properties associated with these points were obtained in each plane. Saddle-point regions associated with spanwise vortices provide the dominant contribution to the Reynolds shear stress and larger contributions to the normal stresses than focal regions. The topology was found to be in close agreement with that obtained from other methods of detecting features of the organized motion. The inter-relationship between critical points simultaneously identified in the two planes can provide some insight into the three-dimensionality of the organized motion. Foci in the (x, z)-plane correspond, with relatively high probability and almost negligible streamwise separation, to saddle points in the (x, y)-plane and are interpreted in terms of ribs aligned with the diverging separatrix between consecutive spanwise vortex rolls. Foci in the (x, z)-plane which correspond, with relatively weak probability, to foci in the (x, y)-plane seem consistent with a distortion of the vortex rolls in the (y, z)-plane.

1. Introduction

The theory of critical points, or points where the velocity is zero and the streamline slope is indeterminate, has been successfully applied to the description of turbulent flow patterns. Lighthill (1963) examined the viscous flow patterns close to a rigid boundary and classified certain critical points that could occur at no-slip boundaries. Smith (1972) applied critical-point theory to the study of conical flows. Perry & Fairlie (1974) addressed the problem of viscous flow and extended this approach to inviscid rotational flows far from boundaries, such as separation bubbles, jets and wakes. Hunt *et al.* (1978) extended the work of Perry & Fairlie, applying it to the study of flows around obstacles attached to surfaces. Using critical-point theory, Cantwell, Coles & Dimotakis (1978) described the conditionally sampled velocity flow fields of turbulent spots. Chong, Perry & Cantwell (1990) generalized the critical-point theory to the classification of three-dimensional flow patterns. More recently, three-dimensional critical-point methodology has been applied to data obtained from direct numerical simulations of both compressible and incompressible turbulent free shear flows (Chen, Cantwell & Mansour 1989; Chen *et al.* 1990; Soria & Cantwell 1993). The approach (see also Hunt, Wray & Moin 1988) uses the invariants of the velocity gradient tensor as the basis for identifying and classifying topological structures.

Complete three-dimensional information on the velocity field is required for interpreting the topology of flow patterns near critical points unambiguously. Such information is not available from experiments. Consequently, a more restrictive

approach is necessary when analyzing experimental data. In the present experiment, two orthogonal arrays provided velocity fluctuations u and v in the (x, y)-plane and u and w in the (x, z)-plane. Two-dimensional critical-point theory is applied to the data obtained in each plane. A critical point which is observed in sectional patterns is not necessarily a critical point in three-dimensional space; only in planes of symmetry, or more generally eigenvector planes, can sectional streamlines be safely interpreted (Perry & Chong 1993). Examples of misinterpretation which may arise when considering only sectional patterns in a plane through a critical point are given by Perry & Chong; for instance, one cannot distinguish between a vortex which is contracting and one which is being stretched. Even when the full three-dimensional velocity field is available, as in the DNS databases, unambiguous identification of vortices remains difficult (Robinson 1991). With the caveat that interpretation should be made with caution, sectional patterns around critical points can nonetheless provide useful insight into the turbulence structure.

To our knowledge, critical points have been usually identified by eye and, consequently, the ensuing description of the flow patterns has been qualitative. In the present work, critical points are identified rigorously on the computer based on the (p, q)-plane classification (e.g. Kaplan 1958; Perry 1984; Perry & Chong 1987) so that flow properties in the vicinity of the critical points can be quantified. The main aim of this work is to describe the contribution of different critical points to the Reynolds stresses and investigate the interrelationship between critical points in the two orthogonal planes, thus permitting possible insight into the three-dimensional nature of flows.

The turbulent near wake of a circular cylinder is considered here. This flow has a high degree of organization and is dominated by spanwise vorticity, implying that vortex lines can be assumed to be approximately normal to the (x, y)-plane. It is therefore attractive for the purpose of clarifying the contribution of the organized motion to turbulent transfer processes. In addition, the convection velocity of vortices for this particular flow has been investigated in detail by Zhou & Antonia (1992). This velocity is essential for the study of critical points as the flow field should be viewed in a frame of reference translating with the vortices. Significant information has already been obtained on the topology of the flow (e.g. Cantwell & Coles 1983; Kiya & Matsumura 1985; Hussain & Hayakawa 1987; Hayakawa & Hussain 1989). On the whole, the information addresses two-dimensional aspects of the organized motion although the experiments of Hayakawa & Hussain (1989) have shown that the organization may be significantly three-dimensional. The present results strengthen some of the suggestions made by Hayakawa & Hussain (1989) in connection with three-dimensional aspects of the organized motion.

2. Experimental details

Experiments were carried out in an open-return low-turbulence wind tunnel with a 2.4 m long working section (0.35×0.35 m). The bottom wall was tilted to obtain a zero streamwise pressure gradient. A circular brass cylinder ($d = 12.5$ mm) was installed in the mid-plane and spanned the full width of the working section, 20 cm from the exit plane of the contraction. This resulted in a blockage of about 3.6% and an aspect ratio of 28. Measurements were made at a constant free-stream velocity ($U_0 = 6.7$ m s^{-1}) at a distance of 20 diameters behind the cylinder. The corresponding Reynolds number Re ($\equiv U_0 d/\nu$) was 5600. In the free stream the longitudinal and lateral turbulence intensities were about 0.05% and 0.08% respectively.

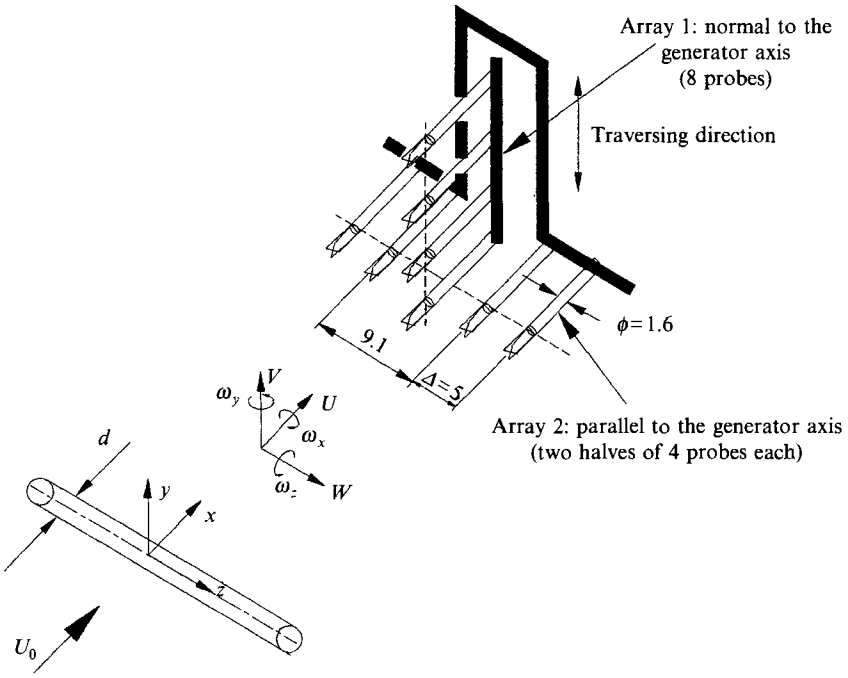

FIGURE 1. Experimental arrangement.

Using two orthogonal arrays, each comprising eight X-wires (figure 1), velocity fluctuations u, v in the (x,y)-plane and u,w in the (x,z)-plane were simultaneously obtained. The arrays were attached to separate traversing mechanisms and could be moved independently of each other. The eight X-wires in the (x,y)-plane were fixed with the second X-wire (from the bottom) at the centreline so that they covered the transverse extent of vortices shed from the upper side of the cylinder, while the eight X-wires in the (x,z)-plane could be displaced in the y-direction and lay at $y/d \approx 0.7$ or 1.2. The nominal spacing between X-wires in both planes was about 5 mm except for a relatively large gap of 9.1 mm between the fourth and fifth X-wires in the (x,z)-plane.

The Wollaston (Pt–10 % Rh) wires (diameter = 5 μm, length ≈ 1 mm) were operated with constant-temperature circuits. Signals from the circuits were offset, low-pass filtered (cut-off frequency = 1.7 kHz), amplified and then digitized using two 16-channel, 12-bit RC A/D boards respectively into two personal computers (NEC 386) at a sampling frequency $f_s = 3.5$ kHz per channel. Data acquisition by the two computers was synchronized using a common external trigger pulse (the configuration is shown in Krogstad, Antonia & Browne 1992). The wires were calibrated for velocity and yaw and continuously checked for drift. Using calibration data, signals proportional to u, v and w, together with the local mean velocities $\bar{U}$, $\bar{V}(\approx 0)$, $\bar{W}(\approx 0)$, were formed and stored on digital tapes. The duration of the digital records was about 38 s. Subsequent data processing was carried out on a VAX 8550 computer.

3. Interference effects

Since a relatively large number of probes were used simultaneously, it was important to minimize the physical blockage due to these probes and ensure that the interference with the flow was small. Miniature ceramic tubes (diameter = 1.6 mm) were used as supports for the X-wires. The resulting blockage caused by the arrays, cables and

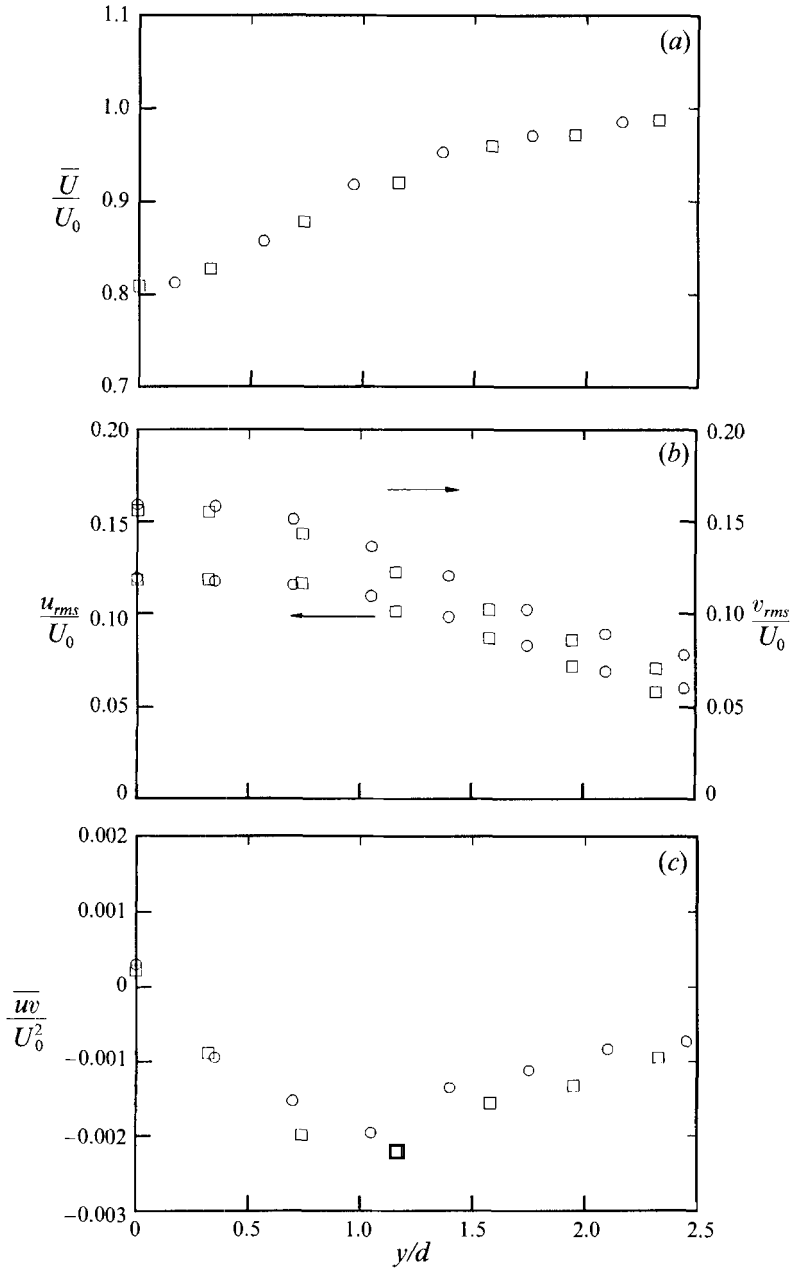

FIGURE 2. Comparison of $\bar{U}$, u_{rms}, v_{rms} and $\overline{uv}$ between the present data (□) and the data (○) from a single X-wire ($x/d = 20$).

supports was estimated to be only about 3 %. Profiles of $\bar{U}$, $(\overline{u^2})^{1/2}$ or u_{rms}, $(\overline{v^2})^{1/2}$ or v_{rms} and $\overline{uv}$ obtained from the X-wires in the (x, y)-plane were compared with those obtained by traversing a single X-wire across the wake. Figure 2 shows that the agreement is quite good for $\bar{U}$, $(\overline{u^2})^{1/2}$, $(\overline{v^2})^{1/2}$ and adequate for $\overline{uv}$. The deviation in $\overline{uv}$ is probably due to experimental uncertainties ($\approx 4\%$) which may appear relatively significant because of the generally small magnitude of $\overline{uv}$, and is not necessarily due to interference of probes with the flow. Measurements were also made with only one

of the arrays, the other one having been removed. The resulting distributions (not shown here) of $\bar{U}$, $(\overline{u^2})^{1/2}$, $(\overline{v^2})^{1/2}$, $(\overline{w^2})^{1/2}$, $\overline{uv}$ and $\overline{uw}$ were in good agreement with those obtained with both arrays. The above tests suggest that the interference of the probes and their support may be assumed to be negligible.

4. Brief background to critical-point theory

A detailed description of critical-point (sometimes phase-plane or phase-space) theory can be found, for example, in Kaplan (1958) and Perry (1984). We only briefly recall here the basic concepts within a two-dimensional framework. Although the discussion is for the (x, y)-plane, it is equally applicable to the (x, z)-plane.

In the neighbourhood of the critical point (x_c, y_c) the nonlinear velocity components $U(x, y)$ and $V(x, y)$ can be approximated by the Taylor series expansions

$$\begin{bmatrix} U \\ V \end{bmatrix} = \begin{bmatrix} a_{11} & a_{12} \\ a_{21} & a_{22} \end{bmatrix} \begin{bmatrix} x \\ y \end{bmatrix} = \boldsymbol{A} \begin{bmatrix} x \\ y \end{bmatrix}, \tag{1}$$

where the origin of the coordinate system is chosen at the critical point, i.e. $x_c = y_c = 0$ and

$$a_{11} = \frac{\partial U}{\partial x}, \quad a_{12} = \frac{\partial U}{\partial y}, \quad a_{21} = \frac{\partial V}{\partial x}, \quad a_{22} = \frac{\partial V}{\partial y},$$

in each case, being evaluated at the origin.

If λ_1 and λ_2 are the eigenvalues of $\boldsymbol{A}$, the corresponding characteristic equation is

$$|\boldsymbol{A} - \lambda \boldsymbol{I}| = 0, \tag{2}$$

where $\boldsymbol{I}$ is the unit matrix. Expanding (2) gives

$$\lambda^2 - p\lambda + q = 0, \tag{3}$$

where
$$q = \det \boldsymbol{A} = a_{11} a_{22} - a_{21} a_{12} \tag{4}$$

and
$$p = \operatorname{tr} \boldsymbol{A} = a_{11} + a_{22}. \tag{5}$$

The latter may be referred to as the velocity divergence in the (x, y)-plane.

The eigenvalues are given by

$$\lambda_{1,2} = \tfrac{1}{2}(p \pm \Delta^{1/2}),$$

where
$$\Delta = p^2 - 4q = (a_{11} - a_{22})^2 + 4a_{21} a_{12}. \tag{6}$$

Critical points which may occur are classified (see Perry 1984) according to the values of p, q and Δ as three non-degenerate types, i.e.

I. saddle-point ($q < 0$),
II. node ($q > 0$, $\Delta > 0$),
III. focus ($\Delta < 0$, $p \neq 0$),

and four degenerate types, including the centre ($q > 0$, $p = 0$). The main interest here is in the three non-degenerate types and one degenerate type, the centre, which are sketched on the (p, q)-chart of figure 3. Streamlines converge to or emanate from foci and nodes depending on whether $p < 0$ or $p > 0$.

The spanwise vorticity ω_z and strain rate s at a critical point in the (x, y)-plane are given by

$$\omega_z = \frac{\partial V}{\partial x} - \frac{\partial U}{\partial y} = a_{21} - a_{12}, \tag{7}$$

$$s = \frac{\partial V}{\partial x} + \frac{\partial U}{\partial y} = a_{21} + a_{12}. \tag{8}$$

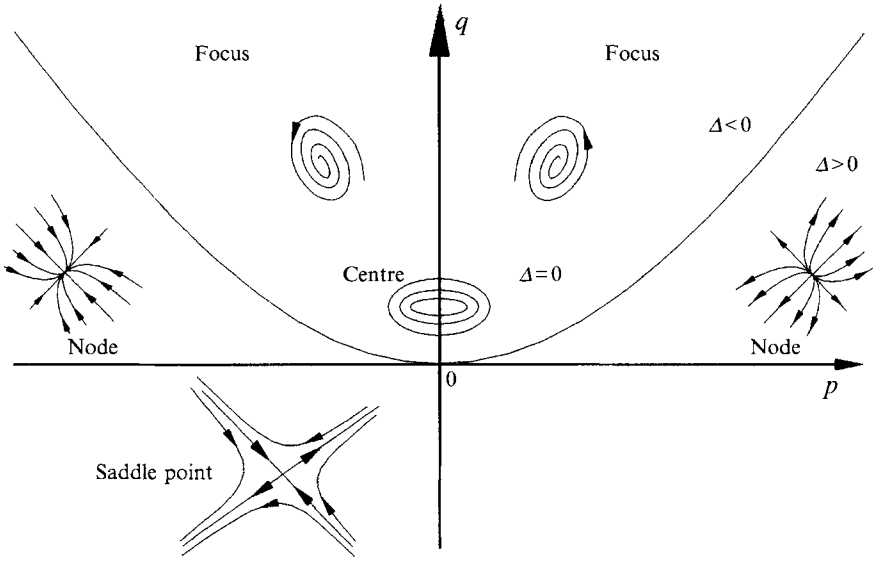

FIGURE 3. Classification of critical points.

If the eigenvalues are real, the corresponding eigenvector slopes are

$$\left.\begin{aligned}\tan\theta_1 &= (\lambda_1 - a_{11})/a_{12} = a_{21}/(\lambda_1 - a_{22})\\ \tan\theta_2 &= (\lambda_2 - a_{11})/a_{12} = a_{21}/(\lambda_2 - a_{22})\end{aligned}\right\}. \tag{9}$$

At a saddle-point, the values of θ_1 and θ_2 give the inclinations to the x-axis of the diverging and converging separatrices through the point.

5. Identification of critical points

In a two-dimensional frame of reference which translates with a convection velocity U_c, the velocity components are given by

$$u_c = U - U_c, \quad v_c = V. \tag{10}$$

The instantaneous signals U and V were formed by adding the local mean velocity values $\bar{U}$ and $\bar{V}$ (≈ 0) to the digital time series of u and v.

The size of the experimental data grid is given by $\Delta x = 1.7$ mm and $\Delta y = 5$ mm (nominal spacing between the X-wires). The value of Δx was identified, using Taylor's hypothesis, with the product $(-\Delta t\, U_c)$, where Δt is the time interval between samples ($\equiv 3500^{-1}$ s). A value of $0.87U_0$ was used for U_c (see §7 for some justification of the value). In view of the disparity in the magnitude of Δx and Δy, data were added at two equispaced y-locations between each pair of existing rows of data. These extra data were obtained by interpolation, based on least-square cubic spline fits to the original data.

Initially, the critical points were assumed to occur when both u_c and v_c changed sign in their time series. To check the validity of these locations, analytical expressions for $u_c(x, y)$ and $v_c(x, y)$ in the vicinity of these points were obtained by applying a surface fit, using a third-order Chebyshev series, to a grid of u_c and v_c data (5 points in both the x- and y-directions) centred at the initial critical point. The final location of a critical point is determined by solving

$$u_c(x_c, y_c) = 0, \quad v_c(x_c, y_c) = 0$$

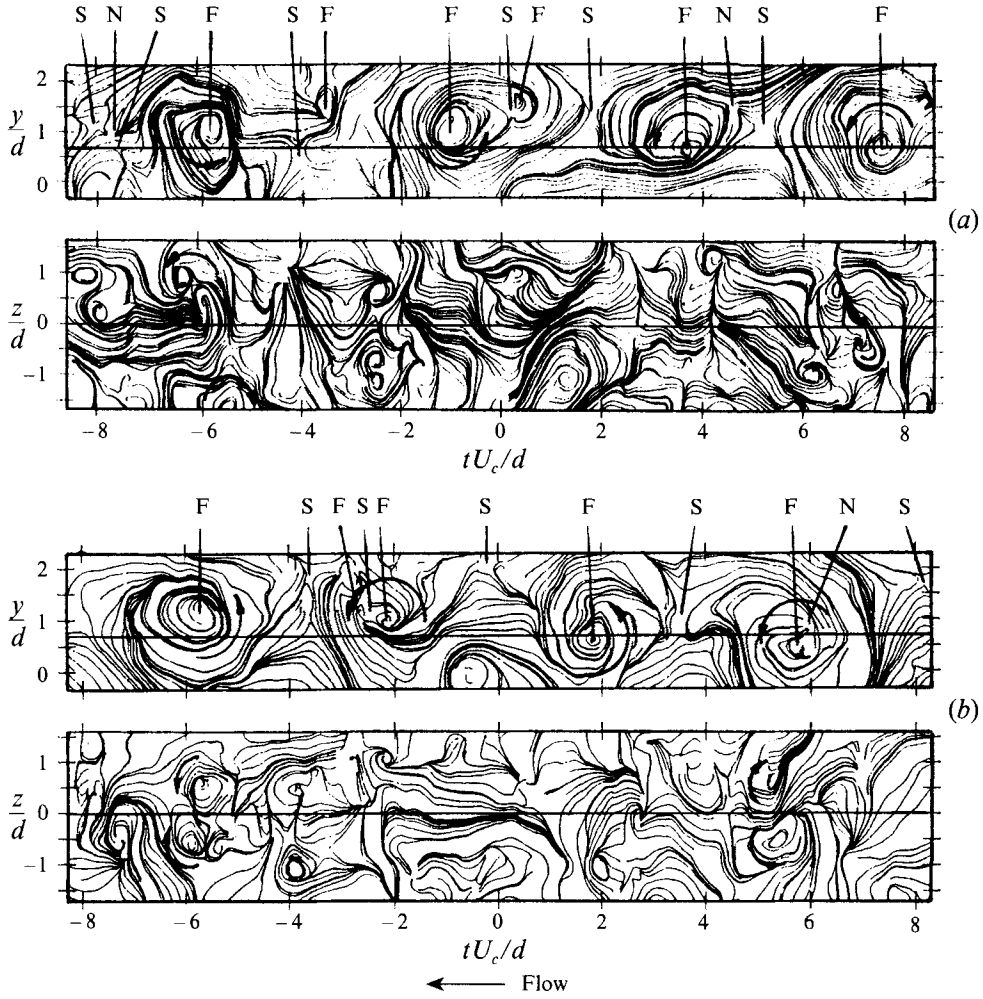

FIGURE 4. Instantaneous sectional streamlines in the (x, y)-plane (upper trace) and (x, z)-plane (lower trace), $y/d = 0.7$, $U_c/U_0 = 0.87$, $t = 0$ is arbitrary. F denotes focus, S saddle-point and N node.

for x_c and y_c. This is done by using a quasi-Newton optimizing algorithm (Gill & Murray 1986) which searches for the minimum of $f = \{[u_c(x, y)]^2 + [v_c(x, y)]^2\}^{1/2}$. When this minimum is significantly small (here, a value of 10^{-3} m s^{-1} was used as the threshold), the corresponding values of x and y are assigned to x_c and y_c. If it is not, the initial critical point is discarded. For those critical points which meet the criterion, velocity derivatives at those points are calculated, thus allowing p, q and Δ to be estimated and the type of a critical point to be determined, as discussed in §4. The location and type of identified critical points are quite consistent with those seen on sectional streamlines, i.e. lines which are tangential to the velocity vectors (e.g. Bisset, Antonia & Browne 1990*b*).

Since the primary interest here is to focus on the relatively large-scale aspects of the organized motion, it was necessary to exclude from the above population of critical points those which may either be associated with small-scale motions or caused, because of the unavoidable spatial jitter of structures, by intersections with one plane of features that belong nominally in the other plane. To implement this elimination, additional criteria were introduced.

For detected foci (with the same sign of ω_z) only one detection was accepted within a certain longitudinal distance of the minimum detecting wavelength λ_d. Initially, λ_d was assumed to be equal to the average shedding wavelength λ_0 but, after inspecting instantaneous sectional streamlines, λ_d was reduced to $0.6\lambda_0$. When several foci occurred within this distance, the one associated with the largest magnitude of Δ (negative) was chosen. This is equivalent to selecting the focus with the largest $|\omega_z|$ since, according to (7), $|\omega_z|$ is large when a_{12} and a_{21} are large in magnitude and opposite in sign, i.e. when Δ, from (6), is most negative. Approximately two-thirds of the number of original foci remained after this criterion was applied.

Saddle-point detections were accepted only when they occurred between two foci (with ω_z of the same sign) that were separated by a distance no greater than $2\lambda_0$. Only the detection with the largest magnitude of s was retained. Approximately two-thirds of the number of original saddle-point detections survived this criterion. No additional condition was used for node detections since the relationship between nodes and aspects of the relatively large-scale motion is unclear.

Examples of the three types of critical points are shown in two sets of instantaneous sectional streamlines (figure 4). In each set, the flow is 'visualized' simultaneously in the (x, y)- and (x, z)-planes. The thick line is each plot denotes the intersection with the other orthogonal plane while arrows about some foci indicate the direction of vorticity which will be used to analyse the configurations of distorted rolls in §9. As a result of the additional criteria, some foci, e.g. at $(tU_c/d, y/d) = (-3.5, 1.4)$, (0.4, 1.5) in figure 4(*a*) and $(-2.6, 1.2)$ in figure 4(*b*), and saddle points, e.g. at $(tU_c/d, y/d) = (-7.5, 0.7)$, (0.2, 1.3) in figure 4(*a*) and $(-2.5, 1.1)$ in figure 4(*b*), are not detected.

6. Conditional and structural averages

The conditional average of an instantaneous quantity F is given by

$$\langle F\rangle_k = \frac{1}{N}\sum_{m=1}^{N} F_{j_m+k}, \tag{11}$$

where k represents time (in samples, positive or negative) relative to the detection points j_m, and N is the total number of detections. (For convenience, the subscript k will be omitted.)

F can be viewed as the sum of the time-mean component $\bar{F}$ and the fluctuation component f. The latter can be further decomposed into the coherent fluctuation $\tilde{f} \equiv \langle f\rangle$ and a remainder f_r, namely

$$f = \tilde{f} + f_r.$$

Also

$$\langle fg\rangle = \tilde{f}\tilde{g} + \langle f_r g_r\rangle, \tag{12}$$

where f and g can each stand for either u or v.

If the conditionally averaged structure begins k_1 samples before the detection instant and ends k_2 samples after this instant, a structural average is denoted by a double overbar, e.g.

$$\langle\overline{\overline{fg}}\rangle = \frac{1}{k_1+k_2+1}\sum_{-k_1}^{k_2}\langle fg\rangle. \tag{13}$$

The value of k_1 $(= k_2)$ is given such that the duration (k_1+k_2+1) corresponds to approximately the average longitudinal extent of regions associated with foci and saddle points.

7. Flow topology and properties associated with critical points†

Since the location of a critical point ($u_c = v_c = 0$) is clearly affected by the choice of the convection velocity (see (10)), it was important to assess the sensitivity of the critical-point location to selected values of U_c. Several methods were used (Zhou & Antonia 1992) to determine the variation of U_c across the wake; the results showed that U_c increased from about $0.85U_0$ at the same centreline to $0.92U_0$ near the edge of the wake, this variation being approximately independent of the method used. One way of quantifying the effect of U_c on the critical-point coordinates is to compare instants at which critical points are identified using different U_c values. The comparison is illustrated here via the probability of the difference between the detection instants of these points corresponding to $U_c = 0.85U_0$ and $U_c = 0.92U_0$, i.e. the extreme values of U_c which are likely to be encountered. The relative probability shown in figure 5 is normalized so that the maximum value is unity. For foci, this value occurs at $t = 0$; the probability has fallen to about 0.1 for the $t = \pm 1$ sample, implying that the error in estimating the focus location is quite small. For saddle-points and nodes, the spread in the probability is slightly greater but the peak remains sharp, suggesting that the overall effect of the U_c variation is small. This is not surprising since at $x/d = 20$, the r.m.s. values of u_c and v_c on the centreline are about $0.12U_0$ and $0.16U_0$ respectively, i.e. nearly one order of magnitude larger than the largest excursions of U_c ($\approx \pm 0.03U_0$). Therefore, any variation in U_c is unimportant relative to the velocity field (u_c, v_c). In addition, the circumferential velocity distribution within the vortices is similar to that of an Oseen vortex (Zhou & Antonia 1993*a*), i.e. it increases appreciably near the vortex centre, implying that the variation in the focus location caused by uncertainty in U_c will be minimized. This may explain why the error in estimating the focus location is smallest. Because the resolution in determining the lateral position y_c of critical points is relatively poor (refer to the size of the experimental data grid in §5), the effect of U_c on y_c has not been investigated. However, it seems unlikely that this effect will differ significantly from that on x_c, or the detection instant. The final choice of U_c was $0.87U_0$, which occurs at the most probable vortex location (Hussain & Hayakawa 1987; Zhou & Antonia 1992), and all subsequent results in the (x, y)-plane were obtained for this value of U_c.

Following the application of the additional criteria introduced in §5, about 3600 foci remained in each plane and the corresponding Strouhal number is 0.18, close to the shedding Strouhal number (≈ 0.2 for the present Reynolds number). The remaining number of saddle-points was somewhat smaller (about 2800 in each plane). Foci and saddle-points dominated the critical-point population, although the number of nodes was not insignificant, about 800 in the (x, y)-plane and 1600 in the (x, z)-plane. Further statistics and properties associated with critical points are presented in Zhou & Antonia (1993*b*).

Figure 6 shows the probability density functions (p.d.f.s) of ω_z, s and p at critical points in the (x, y)-plane. The p.d.f. of ω_z at foci is skewed with its mode at $\omega_z d/U_0 \approx -1.5$, whereas the p.d.f.s at saddle points and nodes are centred near zero and show less spread, i.e. the flow around these points is approximately irrotational. The strain rate at saddle points is large, the mode occurring at $sd/U_0 \approx 0.8$. The bimodal shape of s suggests that above the centreline a small number of saddle points may have a negative strain rate. The distributions of s-values at foci and nodes appear

† Unless otherwise stated, the results in both the (x, y)- and (x, z)-planes are only presented for critical points associated with the structures of negative vorticity since critical points associated with the structures of positive vorticity do not show different features.

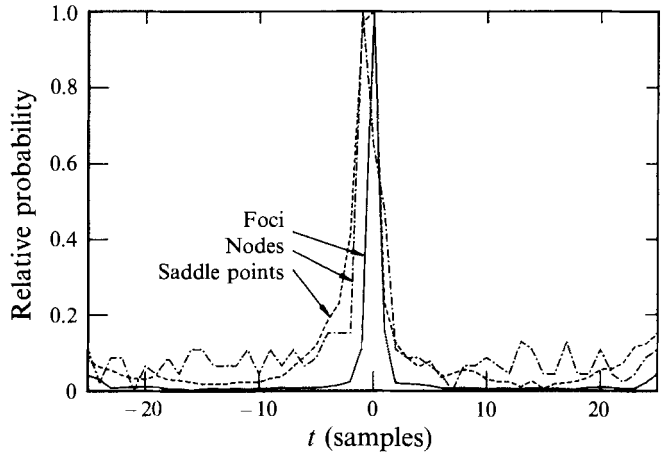

FIGURE 5. Relative probability of length of time between detections of critical points for $U_c = 0.92U_0$ and $U_c = 0.85U_0$ ($t = 0$ is the detection instant for $U_c = 0.85U_0$).

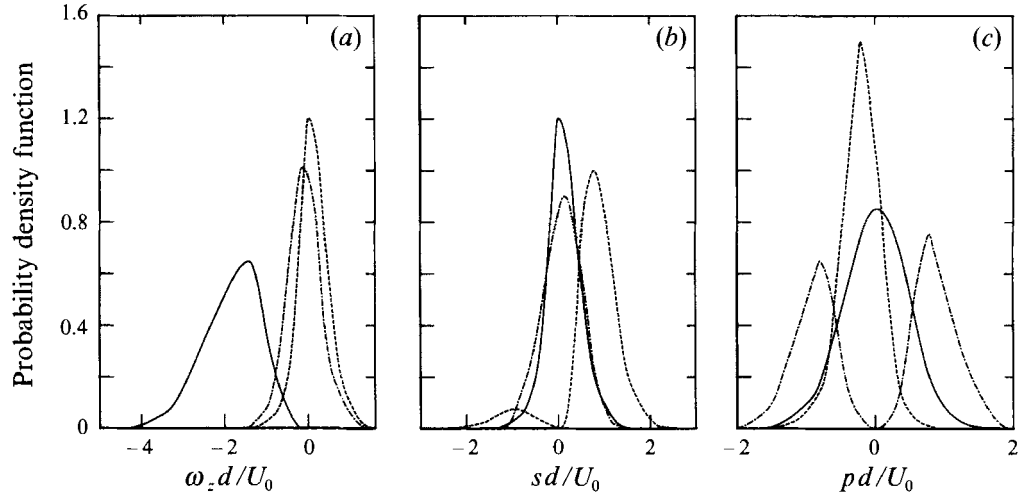

FIGURE 6. Probability density functions (smoothed) of flow properties at foci (——), saddle-points (– – –) and nodes (—·—). (*a*) $\omega_z d/U_0$; (*b*) sd/U_0; (*c*) pd/U_0.

to be more concentrated near zero, indicating that the flow near these points is not highly strained.

Before examining the p.d.f. of the velocity divergence p, some discussion of its implication seems appropriate. For $p > 0$, the continuity equation $\partial u/\partial x + \partial v/\partial y + \partial w/\partial z = 0$ requires that $\partial w/\partial z$ is negative, implying that fluid emanating from critical points, e.g. fluid spiralling out of foci (figure 3), in the (x, y)-plane is due to a spanwise flow deficiency. Conversely, for $p < 0$, $\partial w/\partial z > 0$, implying that part of the spanwise flow originates from fluid which converges towards critical points, e.g. fluid spiralling into foci (figure 3), in the (x, y)-plane. In other words, a non-zero p implies either a deficiency or surplus in spanwise flow, i.e. a local three-dimensionality. A zero p implies a local two-dimensionality. Figure 6(*c*) shows that the p.d.f. of p at foci is approximately Gaussian and centred on zero. This suggests that, locally, the flow near foci is most likely to be almost two-dimensional, i.e. foci degenerate into centres (figure

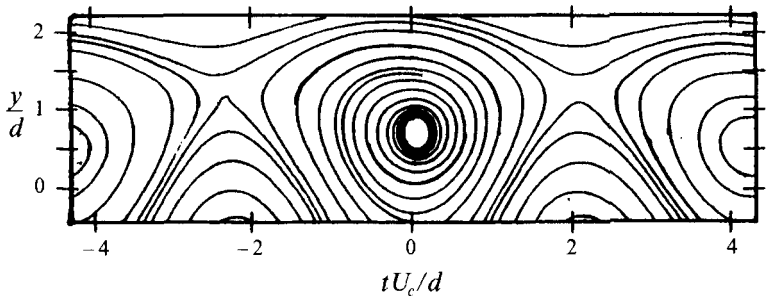

FIGURE 7. Conditional sectional streamlines based on focus detections for $0.5 < y/d < 0.9$.

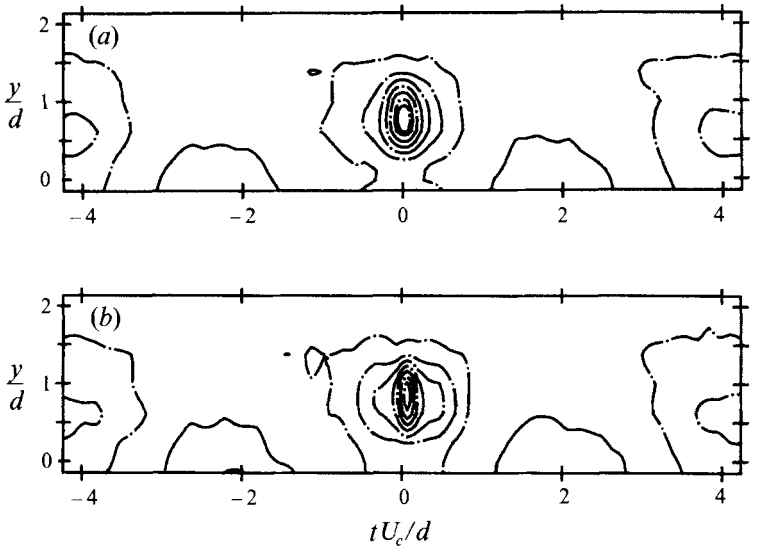

FIGURE 8. Contours of $\langle\omega_z\rangle d/U_0$ based on (*a*) foci: -1.1 to 0.1, step = 0.2, and (*b*) vorticity detections: -1.3 to 0.1, step = 0.2. (Dashed and solid lines represent negative and positive contours respectively.)

3) and the probability that $p > 0$ is almost equal to that for $p < 0$. For saddle-points, the distribution of pd/U_0 has a mode at $pd/U_0 \approx -0.2$, implying an excess of spanwise flow near saddle points. This seems consistent with the existence of a pressure maximum at saddle points (Perry 1984). This pressure maximum tends to drive fluid away from saddle points. The p.d.f. of p is bimodal at nodes – the peaks occur at $pd/U_0 \approx \pm 0.8$ – suggesting that the flow near these points is strongly three-dimensional.

Conditional sectional streamlines based on detected foci near the most probable location ($y/d = 0.5$–0.9) in the (x, y)-plane are shown in figure 7 (the same scales are used in the x- and y-directions in order to avoid any distortion of the physical space). These streamlines exhibit the familiar Kámán vortex tree topology, virtually identical to those (not shown) based on vorticity detections (Zhou & Antonia 1993*a*). This topological similarity is also observed in conditional vorticity contours (figure 8). Evidently, foci coincide with peak vorticity locations, i.e. vortex centres. Since the vorticity detection focuses on vorticity, the corresponding contours (figure 8*b*) are more concentrated with a maximum magnitude slightly higher than in figure 8(*a*).

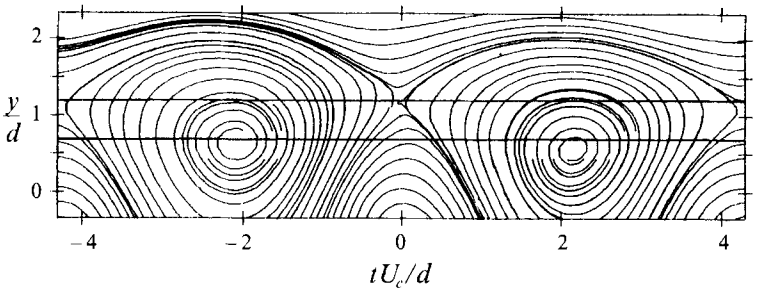

FIGURE 9. Conditional sectional streamlines based on saddle-point detections for $1.0 < y/d < 1.4$. (Solid lines denote the positions of the (x, z)-plane referred to in later figures.)

The conditional sectional streamlines (figure 9) based on saddle points near the most probable location ($y/d = 1.0$–1.4) in the (x, y)-plane exhibit a topology similar to that of figure 7, except for streamwise displacement. Sectional streamlines based on WAG (window average gradient) detections (see Antonia & Fulachier 1989; Bisset *et al.* 1990*b*) in the v-signal at $y = 0.7d$ are very similar (not shown). The separatrix angles θ_1 and θ_2 at the saddle point are about $\pm 50°$, in good agreement with their modes indicated by the p.d.f.s (not shown) of θ_1- and θ_2-values. For irrotational flow ($\omega_z = 0$), the converging and diverging separatrices should be orthogonal (Perry 1984). The fact that the value of $(\theta_1 - \theta_2)$ is slightly greater than 90° is probably associated with the existence of weak vorticity at the saddle points (see figure 6*a*).

8. Contributions to the Reynolds stresses associated with foci and saddle points

In order to quantify the contributions that foci and saddle-point regions make to the Reynolds stresses, these regions should first be characterized in a way that does not depend on the observer. Soria & Cantwell (1993) applied a three-dimensional critical-point classification to each point in free shear flows using DNS databases. They identified strain-rate dominated regions and vortex-like structures from the invariants P, Q and R of the velocity gradient tensor. A similar approach is adopted here by applying a two-dimensional critical-point classification scheme to the data in the (x, y)-plane. In this case, the matrix invariants corresponding to the velocity gradient tensor are now p and q (see (4) and (5)); their values characterize the local topology of the fluid motion at each point in the flow (figure 3). We may identify saddle-point regions with $q < 0$ and focal regions with $\Delta < 0$. Note that the identification of these two regions is invariant with respect to the reference frame.

Iso-contours of $\langle \Delta \rangle$ and $\langle q \rangle$ which are based on focus detections are shown in figure 10. The focal region, identified by $\langle \Delta \rangle \leqslant 0$ (hatched area in figure 10*a*), is considerably elongated laterally, probably due to the spread in the lateral location of foci. This is reflected in the iso-contours of $\langle \Delta \rangle$ (figure 11) based on foci detected near the most probable location ($y/d = 0.5$–0.9). These contours exhibit less elongation because of a smaller variation in the lateral location of foci than in figure 10. Zhou & Antonia (1993*a*) observed that the maximum circumferential velocity around the vortex centre occurs at a radius of about $0.5d$. This radius corresponds approximately to the contour of $\langle \Delta \rangle = 0$ in figure 11, suggesting a correspondence between the boundary of the focal region and the maximum circumferential velocity, which is sometimes used to identify the boundary of vortices (e.g. Hussain & Hayakawa 1987). Note also that the focal

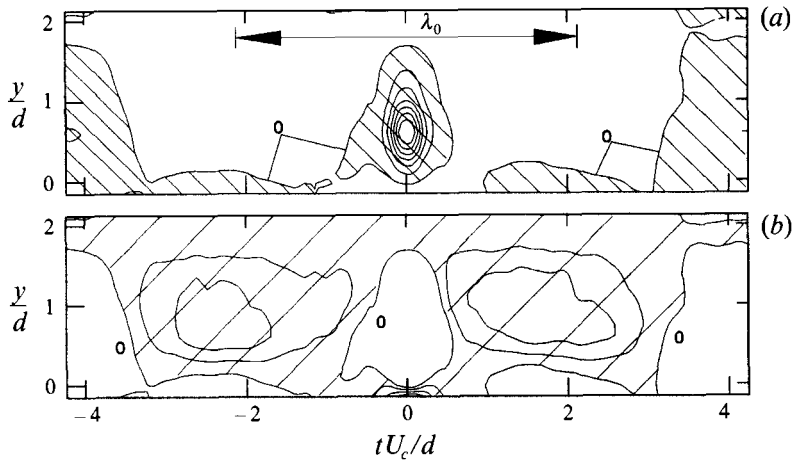

FIGURE 10. (*a*) Iso-contours of $\langle\Delta\rangle\, d^2/U_0^2$ based on focus detections: -0.6 to 0, step $= 0.1$. (*b*) Iso-contours of $\langle q\rangle\, d^2/U_0^2$ based on focus detections: -0.015 to 0, step $= 0.005$.

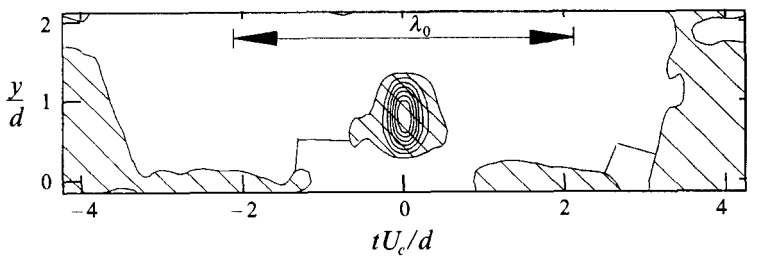

FIGURE 11. Iso-contours of $\langle\Delta\rangle d^2/U_0^2$ based on focus detections between $y/d \approx 0.5$–0.9: -1.2 to 0, step $= 0.2$.

region is associated with a high concentration of vorticity (cf. figure 8*a*). It seems therefore reasonable to associate the focal region with the vortical region.

The saddle-point region, identified by $\langle q\rangle \leqslant 0$ (hatched area in figure 10*b*), is much larger than the focal region. It appears that, collectively, the focal and saddle-point regions account for all the space within one wavelength (λ_0). This is also verified by iso-contours of $\langle\Delta\rangle$ and $\langle q\rangle$ which are based on saddle-point detections (not shown). However, the boundary between the regions indicated by the contours is not identical to that in figure 10, i.e. the iso-contours of $\langle\Delta\rangle$ and $\langle q\rangle$ are, albeit to a small extent, sensitive to different detections. A reasonable estimate of the boundary between focal and saddle regions is the average spatial extent determined from the iso-contours of $\langle\Delta\rangle = \langle q\rangle = 0$ based on focus and saddle-point detections.

As indicated in figure 10, focal regions do not occupy the same amount of space as saddle-point regions. Contributions to the Reynolds stresses ($\overline{fg}$) from each region may be estimated by weighing structural averages in proportion to the longitudinal extent λ of each region, namely

$$\langle\overline{fg}\rangle_f^* = [\lambda_f/\lambda_0]\langle\overline{fg}\rangle_f,$$
$$\langle\overline{fg}\rangle_s^* = [\lambda_s/\lambda_0]\langle\overline{fg}\rangle_s,$$

where the asterisk denotes the contribution to the Reynolds stresses from either region and the subscripts f and s refer to foci and saddle-points respectively.

The value of $\langle\overline{fg}\rangle_{sum}^* = \langle\overline{fg}\rangle_f^* + \langle\overline{fg}\rangle_s^*$ (figure 12) is approximately equal to $\overline{fg}$, the

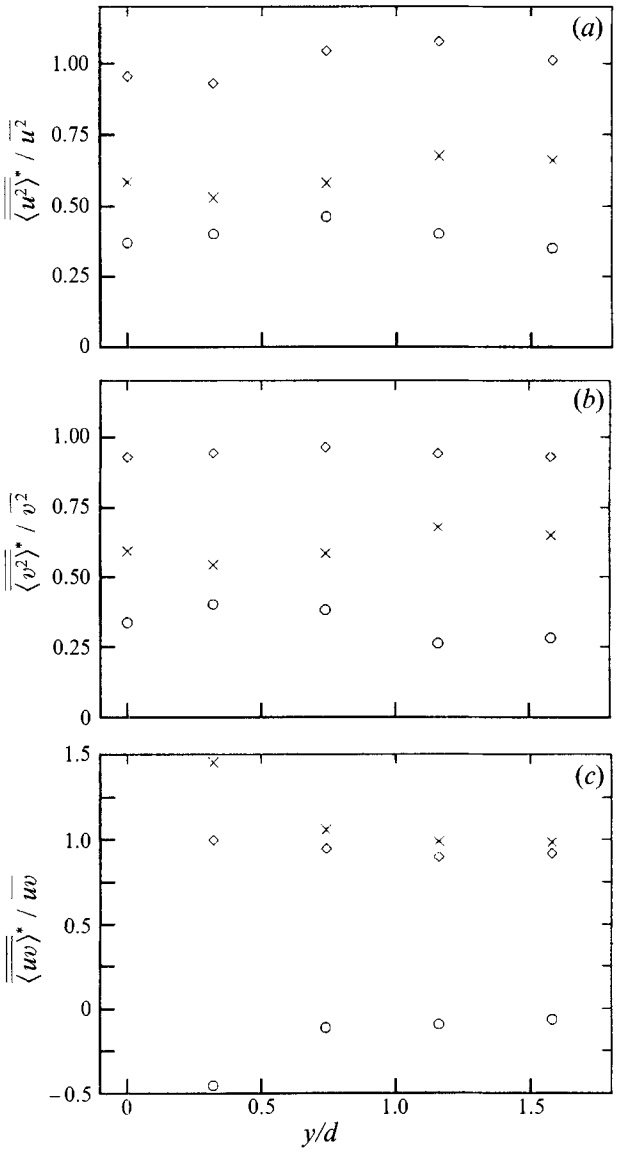

FIGURE 12. Lateral distributions of $\langle\overline{\overline{fg}}\rangle^*/\overline{fg}$ for the focal region (○), the saddle-point region (×) and their sum (◇).

departure being within 10% of $\overline{fg}$. This suggests that, for Reynolds stresses at least, the combination of the selected focal and saddle-point regions is representative of the flow. In neither region does $\langle\overline{\overline{u^2}}\rangle^*/\overline{u^2}$ and $\langle\overline{\overline{v^2}}^*\rangle/\overline{v^2}$ vary greatly with y, but $\langle\overline{\overline{uv}}^*\rangle/\overline{uv}$ does vary, particularly near the centreline where $\overline{uv}$ is small (refer to figure 2*c*). The contribution to the total (time-averaged) Reynolds stresses is greater in the saddle-point than in the focal region. For the saddle-point region, $\langle\overline{\overline{u^2}}\rangle^*/\overline{u^2}$ and $\langle\overline{\overline{v^2}}\rangle^*/\overline{\overline{v^2}}$ are in the range 55–65%, whereas foci contribute 25–45%. The saddle-point region contributes more than 90% to $\overline{uv}$, the foci making only a negligible contribution. The slight negative value of $\langle\overline{\overline{uv}}\rangle_f^*$ is probably due to the influence of the saddle-point region on the other side of the wake. As y/d increases, the influence weakens and the magnitude of $\langle\overline{\overline{uv}}\rangle_f^*$ decreases. While the focal region is associated with a high concentration of vorticity,

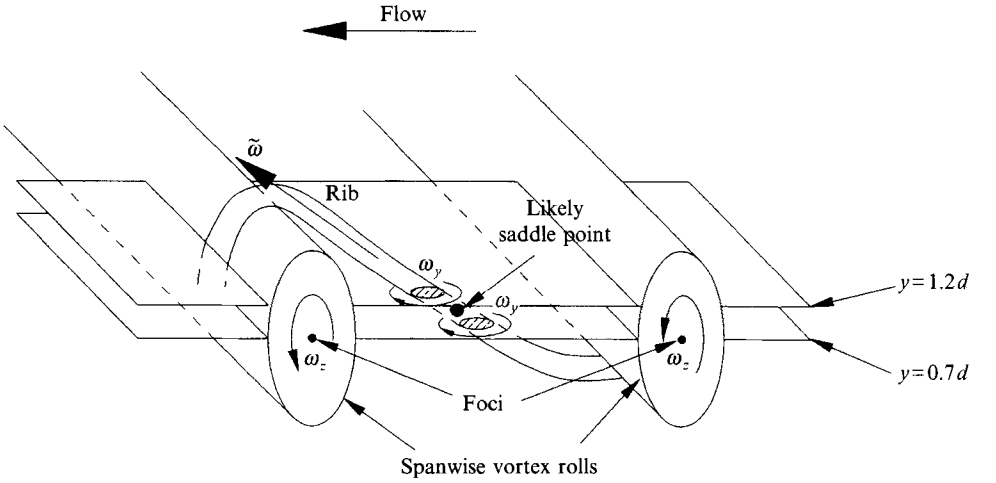

FIGURE 13. Possible spatial configuration of rib (adapted from Hayakawa & Hussain 1989).

the saddle-point region may be identified with the shear-stress or strain-rate bearing region. This does not signify that the vortical region is not important in the context of forming $\overline{uv}$; on the contrary, it may play a major role in setting up the strain field.

9. Some three-dimensional considerations

Previous research on turbulent near wakes has revealed two main types of vortical structures which contribute to the three-dimensionality of this flow. One of these is a quasi-two-dimensional vortex roll with predominantly spanwise vorticity. The other generally lies in the (x, y)-plane and has vorticity components in the x- and y-directions only. It has been suggested (e.g. Kiya & Matsumura 1988; Hayakawa & Hussain 1989) that the latter structures are in the form of ribs which are inclined in the (x, y)-plane and either wrap around or connect successive spanwise structures or rolls. While flow visualizations in near wakes (Meiburg & Lasheras 1987; Williamson 1988) at low Reynolds numbers point to the presence of ribs, there does not appear to be any evidence (either through flow visualizations or more directly through vorticity measurements) for their existence at high Reynolds numbers.

If ribs are indeed inclined in the (x, y)-plane, they should intersect the (x, z)-plane between successive rolls, as sketched for example in figure 13 (see Hayakawa & Hussain 1989). These intersections should coincide with concentrations of vorticity or foci. The simplified sketch shows that the streamwise location of these foci coincides approximately with the saddle-point region in the (x, y)-plane. The relative probability of the length of time between saddle-points in the (x, y)-plane and foci in the (x, z)-plane is shown in figure 14, the reference time ($tU_c/d = 0$) corresponding to the instant at which the saddle-points are detected. Note that the peak probability does indeed occur near the origin. The time delay between the two peaks corresponding to the two (x, z)-plane locations suggests an inclination to the x-axis of about 55°. This angle differs only slightly from that ($\approx 50°$) of the diverging separatrix through the saddle point. One may surmise that the ribs are approximately aligned with the diverging separatrix, although slightly upstream from it. It should be remembered that in figure 14 the foci in the (x, z)-plane can be anywhere within the span of the probes; it is only the time duration that is considered.

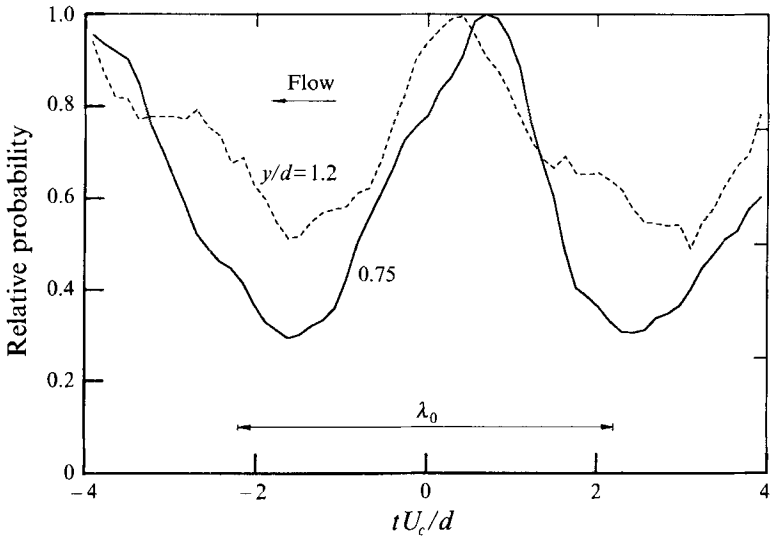

FIGURE 14. Relative probability (smoothed) of length of time between saddle-points in the (x, y)-plane and foci in the (x, z)-plane ($tU_c/d = 0$ is the instant at which saddle-points are detected).

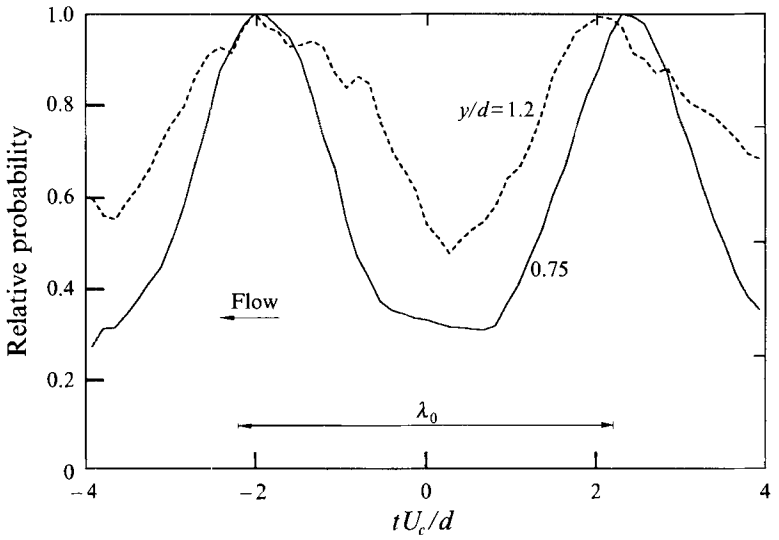

FIGURE 15. Relative probability (smoothed) of length of time between foci in the (x, y)- and (x, z)-planes ($tU_c/d = 0$ is the instant of foci detection in the (x, y)-plane).

Figure 15 shows the relative probability of the length of time between foci in the (x, y)- and (x, z)-planes, the reference time ($tU_c/d = 0$) being the instant at which foci in the (x, y)-plane are detected. The peaks occur about half a wavelength apart from $tU_c/d = 0$, i.e. in the saddle-point region, consistent with figure 14, whereas the minima occur near foci ($tU_c/d = 0$) in the (x, y)-plane. The non-negligible magnitudes of the minima indicate that foci in the (x, z)-plane may occur simultaneously with foci in the (x, y)-plane. The two illustrations in figure 16 (see Hayakawa & Hussain 1989 and Bisset, Antonia & Britz 1990*a*) are consistent with this possibility. However, they may not be the only possibility. Others, such as independent structures that just happen to be nearby and vortices inclined, relative to the z-axis, in the (y, z)-plane are also likely.

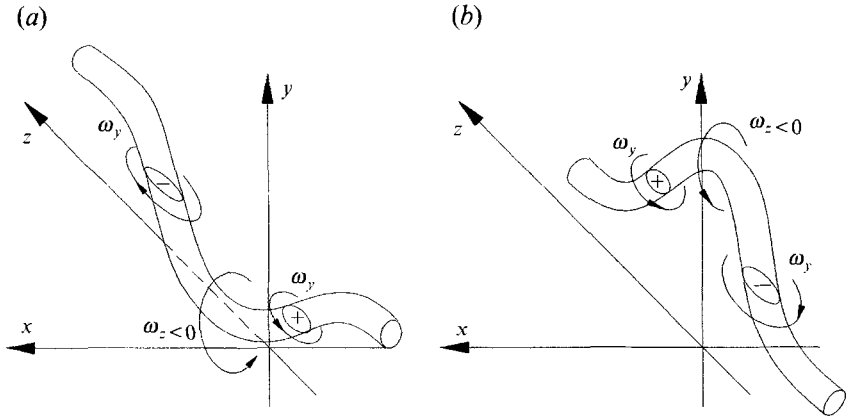

FIGURE 16. Possible spatial configurations of distorted rolls: (*a*) kinked inwards; (*b*) kinked outwards (Hayakawa & Hussain 1989; Bisset *et al.* 1990*a*).

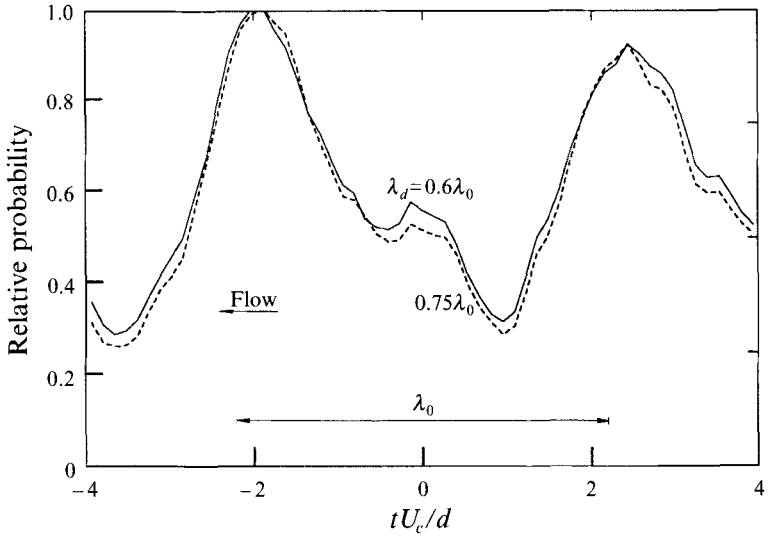

FIGURE 17. Relative probability (smoothed) of length of time between vorticity detections in the (x,y)- and (x,z)-planes $(y/d=0.7)$.

When the vorticity method (Zhou & Antonia 1993*a*) is applied, the relative probability (figure 17) of the time between detections in the (x,y)- and (x,z)-planes is not quite the same as in figure 15. The reference time $(tU_c/d=0)$ in figure 17 corresponds to the instant when vortices in the (x,y)-plane are detected. Prominent peaks occur about half a wavelength apart from $tU_c/d=0$, i.e. in the saddle-point region. This agrees with figure 15. But a smaller peak appears near $tU_c/d=0$. It has been verified that the correspondence between vorticity and focus detections is quite good in the (x,y)-plane but not as good in the (x,z)-plane, i.e. some detectable ω_y concentrations do not seem to correspond to foci. In a turbulent wake, vortex rolls are generally non-uniform and perhaps very short (Bisset *et al.* 1990*a*), which may give rise to a spanwise gradient $\partial u/\partial z$ of u, as indicated by the contours (figure 18) of $\langle u\rangle/U_0$ based on focus detections in the (x,y)-plane. This additional $\partial u/\partial z$, corresponding to the vortex centre, is likely to cause a concentration of $\omega_y(\equiv \partial u/\partial z-\partial w/\partial x)$ without a

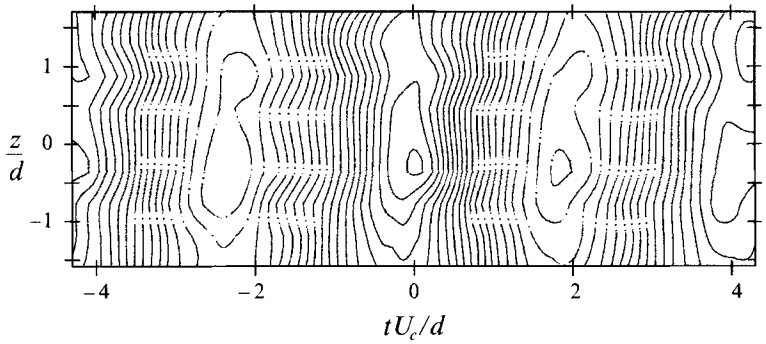

FIGURE 18. Contours of $\langle u \rangle / U_0$ in the (x, z)-plane based on focus detections in the (x, y)-plane: -0.045 to 0.05, step = 0.005. (Dashed and solid lines represent negative and positive contours respectively.)

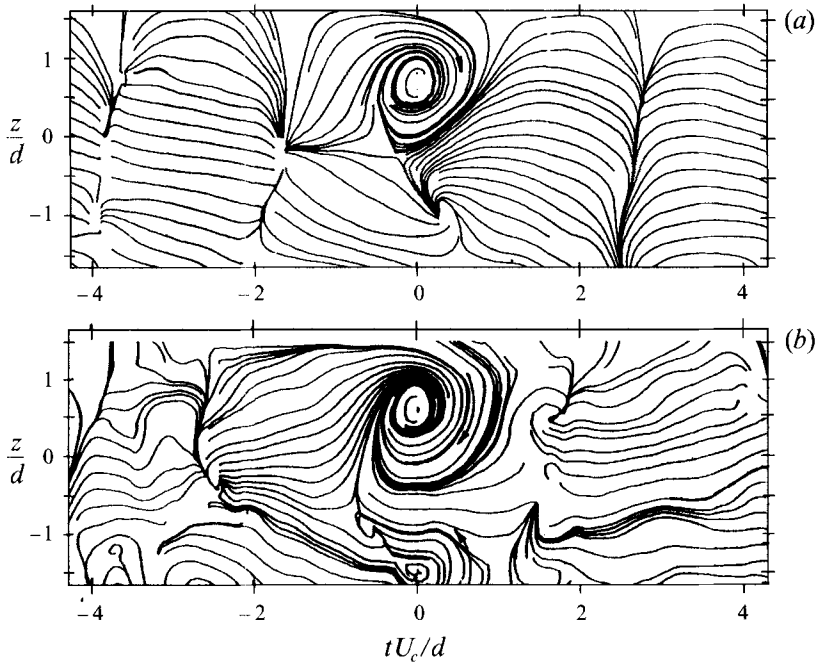

FIGURE 19. Conditional sectional streamlines based on foci $(0.5 < z/d < 1.0)$ in the (x, z)-plane corresponding to (*a*) the peak $(tU_c/d = 0.75)$ in figure 14 and (*b*) the valley $(tU_c/d = 0)$ in figure 15. (Window width = ± 0.25 average shedding wavelength, $t = 0$ is the detection instant, $U_c = 0.87U_0$, $y/d = 0.7$, arrows indicate the direction of vorticity.)

contribution from $\partial w/\partial x$. Such a concentration is not necessarily associated with a focus. This may account for the absence in figure 15 of the minor peak which occurs near $tU_c/d = 0$ in figure 17. The magnitude of this peak, as shown in figure 17, reduces as the minimum detecting wavelength λ_d increases from $0.6\lambda_0$ to $0.75\lambda_0$, suggesting that the ω_y concentration due to the spanwise non-uniformity of vortex rolls is generally weaker than that due to ribs (corresponding to the saddle-point region).

Conditional sectional streamlines in the (x, y)-plane based on detections of foci for $0.5 < z/d < 1.0$ which correspond to either the peak in figure 14 or the valley in figure 15 are shown in figures 19(*a*) and 19(*b*) respectively. The streamlines in figure 19(*a*) reflect, as expected, the presence of vorticity in the vicinity of the detection point; there

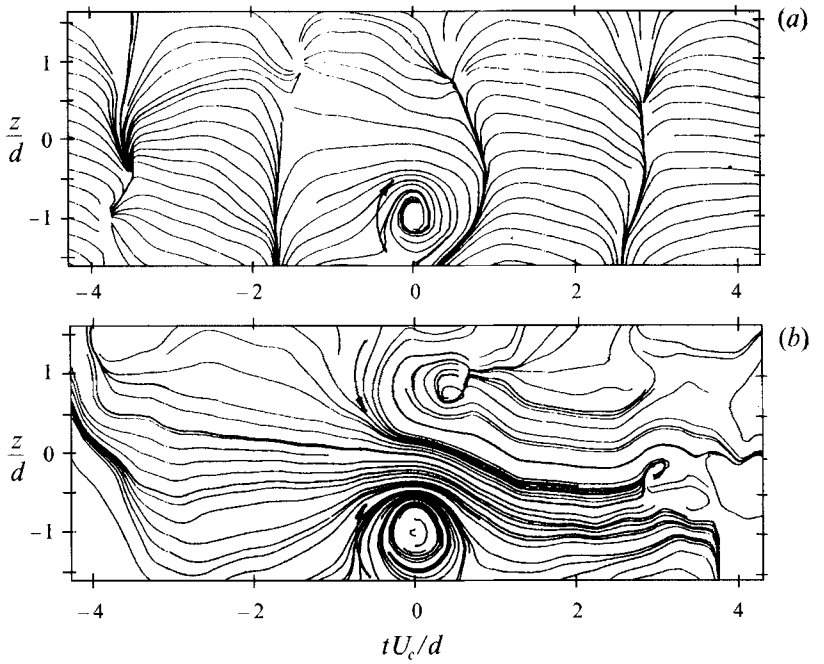

FIGURE 20. Conditional sectional streamlines based on foci ($-1.2 < z/d < -0.7$) in the (x, z)-plane corresponding to (*a*) the peak ($tU_c/d = 0.75$) in figure 14 and (*b*) the valley ($tU_c/d = 0$) in Figure 15. (Window width = ± 0.25 average shedding wavelength, $U_c = 0.87U_0$, $y/d = 0.7$, arrows indicate the direction of vorticity.)

is no evidence however of vortical regions elsewhere in that plane. It would seem that ribs occur with high probability but their occurrence is random in the spanwise direction. Also, the jitter in the longitudinal position is sufficiently important to yield the results in figure 19(*a*). The appearance of the streamlines in figure 19(*b*) reveals a secondary focus at $z/d \approx -1.5$, opposite to the primary focus centred at $z/d \approx +0.75$. The presence of the secondary focus seems consistent with configuration (*a*) in figure 16. Similar observations can be obtained when conditional sectional streamlines (figure 20) are based on detections of foci for $-1.2 < z/d < -0.7$. Apparently, the topology in figure 20(*b*) is in agreement with configuration (*b*). Examples of the two configurations can be identified in the instantaneous data of figure 4. At $tU_c/d \approx -6.3$ (figure 4*a*), one focus at $z/d \approx 0.8$ in the (x, z)-plane has ω_y of opposite sign to the focus at $tU_c/d \approx -5.7$ and $z/d \approx -1.6$. They both appear to be related to the focus at $y/d \approx 1.0$ in the (x, y)-plane and suggest the occurrence of an outwardly kinked roll. At $tU_c/d \approx 5.5$ in figure 4(*b*), two foci in the (x, z)-plane, assuming they are related to the focus at $y/d \approx 0.5$ in the (x, y)-plane, may represent the legs of an inwardly kinked roll. It would thus seem that both configurations in figure 16 are possible in the near wake. We emphasize that these configurations are the least likely of all events, as indicated by the minima in figure 15 and the weak secondary focus (by comparison to the primary focus) in figures 19(*a*) and 20(*b*).

A few curves in figures 19 and 20, particularly figures 19(*a*) and 20(*a*), are clearly identifiable which run approximately in a spanwise direction and divide the flow into distinct regions. It has been verified that the value of $\langle u_c \rangle$ is zero along these curves, i.e. these curves are stagnation curves. They may be referred to as two-dimensional bifurcation lines since two incoming sectional streamlines combine to form one, or two

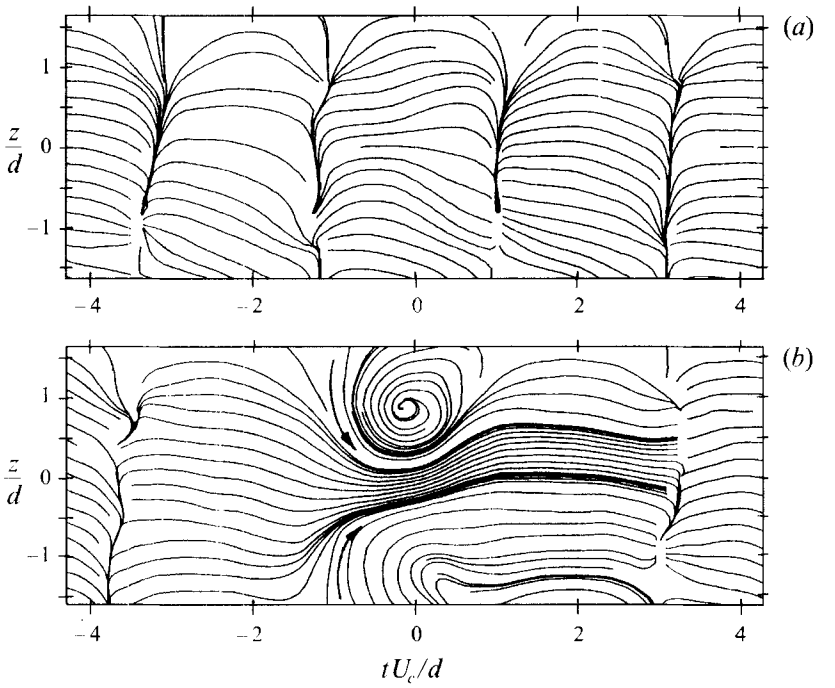

FIGURE 21. Conditional sectional streamlines in the (x, z)-plane ($y/d = 0.7$) based on (a) saddle-points and (b) foci ($1.0 < y/d < 1.4$) in the (x, y)-plane. (Arrows indicate the direction of vorticity.)

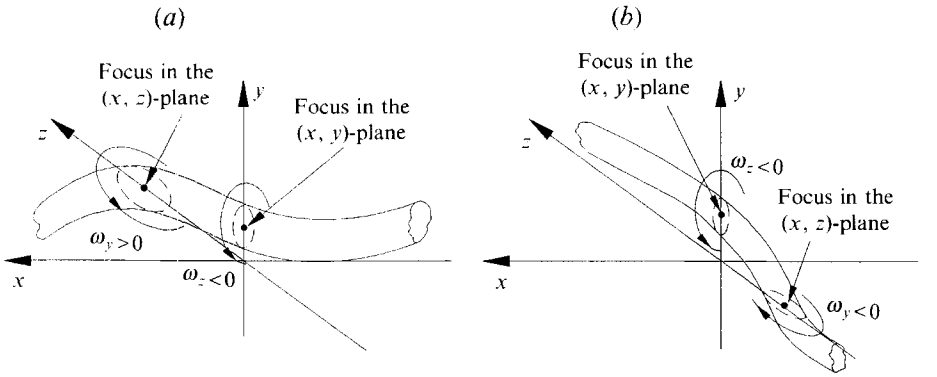

FIGURE 22. Possible configurations of rolls which are inclined in the (y, z)-plane.

outgoing sectional streamlines diverge from a point along these curves. The former is a negative bifurcation, while the latter is a positive bifurcation (Hornung & Perry 1984; Perry & Hornung 1984).

Figure 21 shows a comparison of conditional sectional streamlines in the (x, z)-plane ($y/d = 0.7$) which are based on either saddle-point or focus detections ($1.0 < y/d < 1.4$) in the (x, y)-plane. While streamlines based on saddle-point detections show no evidence of rotational flow regions, corroborating the suggestion that ribs seems to occur randomly, those based on focus detections tend to delineate a pair of counter-rotating vortical regions. The counter-rotating pair seems consistent with the likely three-dimensional nature of the vortex rolls. In particular, it is consistent

with the existence of vortex rolls (figure 22) that are inclined in the (y, z)-plane. (Note that the sketches in figure 22 are not meant to imply that vortex rolls have well-defined boundaries or that their shapes are known precisely; they are only an attempt to interpret the correspondence between foci observed in the (x, y)-plane and those in the (x, y)-plane.)

10. Conclusions

The phase-plane technique has been applied to the identification of critical points from simultaneously sampled measurements in the (x, y)- and (x, z)-planes in the near wake of a circular cylinder. The critical-point population is dominated by foci and saddle points, although the number of nodes was significant. Foci are associated with local vorticity maxima, while saddle points correspond to extrema in the local strain rate. Accordingly, a detection method based on foci yields approximately the same topology as a vorticity-based detection method and a detection method based on saddle points is in close agreement with the WAG detection methods. At nodes, the velocity divergence is large, implying a relatively strong local three-dimensionality.

Regions associated with foci and saddle points can be identified from the values of the invariants p and q. Saddle-point regions are much large in size than focal regions. Correspondingly, the former regions dominate the contributions to the Reynolds stresses. They account for 55–65 % of the Reynolds normal stresses and for more than 90 % of the Reynolds shear stress. Focal regions account for about 25–45 % of the Reynolds normal stresses and make a negligible contribution to the Reynolds shear stress.

The inter-relationship between critical points in the (x, y)- and (x, z)-planes has provided some useful information on the three-dimensionality of the organized motion in the near wake. The most probable location for foci in the (x, z)-plane corresponds, with almost negligible streamwise separation, to the saddle point in the (x, y)-plane. This relationship quantifies the existence of vortical structures (ribs) which lie, on average, in the (x, y)-plane and are approximately aligned in the direction of the diverging separatrix. These structures are more likely to occur randomly (in the spanwise direction) rather than as counter-rotating vortex pairs. The correspondence between foci in the (x, y)-plane and foci in the (x, z)-plane is much less probable than that between saddle points in the (x, y)-plane and foci in the (x, z)-plane. This correspondence may reflect the presence of distorted vortex rolls, e.g. inclined to the z-axis, kinked in the (y, z)-plane. Although the precise shape of the rolls is not known, the likelihood that they are symmetrically kinked, either inwardly or outwardly, would appear to be quite small.

We acknowledge Mr J. Mi's contribution to the experimental work. We are very grateful to Dr D. K. Bisset for his comments and suggestions on the manuscript. The support of the Australian Research Council is appreciated.

REFERENCES

ANTONIA, R. A. & FULACHIER, L. 1989 Topology of a turbulent boundary layer with and without wall suction. *J. Fluid Mech.* **198**, 429–451.

BISSET, D. K., ANTONIA, R. A. & BRITZ, D. 1990*a* Structure of large-scale vorticity in a turbulent far wake. *J. Fluid Mech.* **218**, 463–482.

BISSET, D. K., ANTONIA, R. A. & BROWNE, L. W. B. 1990*b* Spatial organization of large structures in the turbulent far wake of a cylinder. *J. Fluid Mech.* **218**, 439–461.

CANTWELL, B. J. 1978 Similarity transformations for the two-dimensional unsteady stream function equations. *J. Fluid Mech.* **85**, 257–271.

CANTWELL, B. & COLES, D. 1983 An experimental study of entrainment and transport in the turbulent near wake of a circular cylinder. *J. Fluid Mech.* **136**, 321–374.

CANTWELL, B. J., COLES, D. & DIMOTAKIS, P. E. 1978 Structure and entrainment in the plane of symmetry of a turbulent spot. *J. Fluid Mech.* **87**, 641–672.

CHEN, J., CANTWELL, B. & MANSOUR, N. N. 1989 The topology and vorticity dynamics of a three-dimensional plane compressible wake. *Proc. Tenth Australasian Fluid Mechanics Conference, Melbourne*, p. 5.1.

CHEN, J. H., CHONG, M. S., SORIA, J., SONDERGAARD, R., PERRY, A. E., ROGERS, M., MOSER, R. & CANTWELL, B. J. 1990 A study of the topology of dissipating motions in direct numerical simulations of time-developing compressible and incompressible mixing layers. *CTR Proc. Summer Program 1990*, pp. 139–141.

CHONG, M. S., PERRY, A. E. & CANTWELL, B. 1990 A general classification of three-dimensional flow patterns. *Phys. Fluids* A **2**, 767–777.

GILL, P. E. & MURRAY, W. 1976 Minimization subject to bounds on the variations, *Rep.* NAC 72. National Physical Laboratory.

HAYAKAWA, M. & HUSSAIN, F. 1989 Three-dimensionality of organized structures in a plane turbulent wake. *J. Fluid Mech.* **206**, 375–404.

HORNUNG, H. G. & PERRY, A. E. 1984 Some aspects of three-dimensional separation. Part I. Streamsurface bifurcations. *Z. Flugwiss. Weltraumforsch.* **8**, 77–87.

HUNT, J. C. R., ABELL, C. J., PETERKA, J. A. & WOO, H. 1978 Kinematical studies of the flows around free or surface-mounted obstacles, applying topology to flow visualization. *J. Fluid Mech.* **86**, 179–200.

HUNT, J. C. R., WRAY, A. A. & MOIN, P. 1988 Eddies, streams and convergence zones in turbulent flows. *CTR Proc. Summer Program 1988, Rep.* CTR-S88, pp. 193–208.

HUSSAIN, A. K. M. F. & HAYAKAWA, M. 1987 Education of large-scale organized structures in a turbulent plane wake. *J. Fluid Mech.* **180**, 193–229.

KAPLAN, W. 1958 *Ordinary Differential Equations.* Addison-Wesley. pp. 414–423.

KIYA, M. & MATSUMURA, M. 1985 Turbulence structure in intermediate wake of a circular cylinder. *Bull. JSME* **28**, 2617–2624.

KIYA, M. & MATSUMURA, M. 1988 Incoherent turbulence structure in the near wake of a normal plate. *J. Fluid Mech.* **190**, 343–356.

KROGSTAD, P.-Å., ANTONIA, R. A. & BROWNE, L. W. B. 1992 Structure investigation in a turbulent boundary layer using orthogonal X-wire arrays. *Proc. Eleventh Australasian Fluid Mechanics Conf., Hobart*, pp. 251–254.

LIGHTHILL, M. J. 1963 Attachment and separation in three-dimensional flow. In *Laminar Boundary Layers* (ed. L. Rosenhead), pp. 72–82. Oxford University Press.

MEIBURG, E. & LASHERAS, J. C. 1987 Comparison between experiments and numerical simulations of three-dimensional plane wakes. *Phys. Fluids* **30**, 623–625.

PERRY, A. E. 1984 A study of degenerate and nondegenerate critical points in three-dimensional flow fields *Forschungsbericht, Institut für Experimentelle Strömungsmechanik, Göttingen*, p. 63.

PERRY, A. E. & CHONG, M. S. 1987 A description of eddying motions and flow patterns using critical-point concepts. *Ann. Rev. Fluid Mech.* **19**, 125–155.

PERRY, A. E. & CHONG, M. S. 1993 Topology of flow patterns in vortex motions and turbulence. In *Eddy Structure Identification in Free Turbulent Shear Flows* (ed. M. N. Glauser & J.-P. Bonnet), pp. 339–362. Kluwer.

PERRY, A. E. & FAIRLIE, B. D. 1974 Critical points in flow patterns. *Adv. Geophys.* **18** B, 299–315.

PERRY, A. E. & HORNUNG, H. G. 1984 Some aspects of three-dimensional separations. Part II. Vortex skeletons. *Z. Flugwiss. Weltraumforsch.* **8**, 155–160.

ROBINSON, S. K. 1991 Coherent motions in the turbulent boundary layer. *Ann. Rev. Fluid Mech.* **23**, 601–639.

SMITH, J. H. B. 1972 Remarks on the structure of conical flow. *Prog. Aeronaut. Sci.* **12**, 241–272.

SORIA, J. & CANTWELL, B. J. 1993 The identification and classification of topological structures in free shear flows. In *Eddy Structure Identification in Turbulent Shear Flows* (ed. M. N. Glauser & J.-P. Bonnet), pp. 379–390. Kluwer.

WILLIAMSON, C. H. K. 1988 The existence of two stages in the transition to three-dimensionality of a cylinder wake. *Phys. Fluids* **31**, 3156–3168.

ZHOU, Y. & ANTONIA, R. A. 1992 Convection velocity measurements in a cylinder wake. *Exps Fluids* **13**, 63–70.

ZHOU, Y. & ANTONIA, R. A. 1993*a* A study of turbulent vortices in the near wake of a cylinder. *J. Fluid Mech.* **253**, 643–661.

ZHOU, Y. & ANTONIA, R. A. 1993*b* A study of flow properties near critical points. In *Eddy Structure Identification in Free Turbulent Shear Flows* (ed. M. N. Glauser & J.-P. Bonnet), pp. 137–150. Kluwer.